

Real-time implementation of optimal operation of single-stage grid interfaced PV system under weak grid conditions

ISSN 1751-8687
 Received on 21st April 2017
 Revised 17th October 2017
 Accepted on 30th November 2017
 E-First on 19th February 2018
 doi: 10.1049/iet-gtd.2017.0623
 www.ietdl.org

Priyank Shah¹ ✉, Ikhtlaq Hussain¹, Bhim Singh¹

¹Department of Electrical Engineering, Indian Institute of Technology Delhi, New Delhi 110016, India

✉ E-mail: p4priyank1504@gmail.com

Abstract: This study presents a real-time implementation of the optimal operation of a single-stage three-phase grid interfaced solar photovoltaic (PV) system with active shunt filter capabilities. The control approach is based on the least logarithmic absolute difference with an adaptive filtering technique. It serves manifold objectives of power quality improvements in the distribution network as well as grid side abnormalities such as voltage distortions, voltage sag and voltage swell. The proposed control algorithm has advantages of better steady state as well as dynamic performances as compared to conventional algorithms. The perturb and observe-based maximum power point tracking algorithm is used to harness crest power from the PV array. The proposed system is simulated in MATLAB/Simulink platform using Simscape power systems toolbox and its performance is compared with conventional algorithms. A prototype of the proposed system is developed in the laboratory and its responses are found satisfactory under various operating conditions such as load unbalancing, reactive power compensation, variable solar insolation, voltages distortion, voltage sag and voltage swell. The total harmonic distortions of grid currents and grid voltages are found within limits of an IEEE-519 standard.

1 Introduction

Due to the use of fossil fuels for energy generation, adverse effects are occurred on the environment such as ozone depletion, greenhouse gas emission and acid rain [1]. Now-a-days, the policies for renewable power generation support the capital subsidies to promote its applications and to provide subsidies in taxes [2]. Due to innovation in research and technology improvement in manufacturing, the cost of photovoltaic (PV) array is decreasing day by day. Hence, reliability of PV array in miniature scale applications is improved [3].

Various methods are available to model and simulate the PV array [4, 5]. Kaplani *et al.* [6] have examined the effects of humidity, inclination and orientation of PV modules, rapid change in solar insolation on output of PV array, which are analysed for various conditions. Therefore, maximum power point tracking (MPPT) algorithm must be fast, reliable, less complex and adaptive at varying atmospheric conditions, which enhances the penetration of PV array-based generation into the grid by extracting maximum power from PV array. Various classical and artificial neural network techniques for standalone system, combination of these techniques with classical MPPT algorithms and hybrid techniques, are analysed with their complexity, convergence speed and accuracy. Moreover, an implementation of various MPPT methods is described in [7, 8].

The power loss analysis is carried out for different operating conditions such as fast insolation variation and double line frequency voltage ripple. Different compositions of it are analysed for single-stage and double-stage topologies for three phase grid interfaced PV system and variety of advantages over double-stage topology [9], are as follows:

- i. Numbers of components used in single-stage topology (diodes and capacitors etc.) are less. Therefore, weight, complexity and cost of topology are reduced.
- ii. Efficiency of the single-stage topology is high due to reduced losses.

Moreover, various conventional algorithms such as generalised integrators enhanced phase locked loop are reported in [10] to extract fundamental component from the distorted signal. Many

algorithms such as quadrature-phase locked loop [11], least mean fourth (LMF) [12], variable step size least mean square (VSS-LMS) [13], peak estimation [14] are demonstrated for interaction between PV system with three-phase grid with active shunt filtering capabilities. Owing to the double frequency oscillation problem and poor dynamic response carried by lowpass filter in synchronous reference frame (SRF)-based phase locked loop, the performance of the system is degraded. However, second-order generalised integrator and second-order generalised integrator quadrature have lower harmonics and DC offset filtering capabilities, respectively. Due to slow convergence during steady-state operations, performance of the solar PV system is not reliable for conventional LMF and VSS-LMS algorithms, respectively. The behaviour of system using peak estimation technique is not reliable due to poor dynamic response as the lowpass filter is used in path of fundamental extraction of non-linear load current. The single layer neural network-based control scheme is proposed in [15] for double-stage grid interfaced solar PV array system to improve power quality of the system. The double-stage topology has low-power transfer efficiency due to additional losses in the boost converter. The parallel operation of two single-stage solar PV system is modelled and analysed in [16] to improve the power quality of the distribution network along with droop characteristics. The ideal magnitude and phase characteristics of notch filter [17] make it complex in real-time implementation of solar PV grid interfaced system. Moreover, sensitive performance parameters variations of the system make it least feasible for the practical applications of solar PV grid interfaced system. Therefore, there is a need for adaptive filtering algorithm, which can enhance the system performance without affecting system topology.

An adaptive filter theory has been demonstrated based on relative logarithmic cost function which has capabilities of higher and lower order error into a single incessant update in [18]. The least logarithmic absolute difference (LLAD) algorithm belongs to the family of adaptive filters. Under impulsive interference environment, the convergence of LLAD algorithm is better than the LMF algorithm. The LLAD algorithm has high convergence speed than the LMS and sign algorithm. The error associated with this algorithm is introduced by means square error, mean square deviation (MSD) and its comprehensive analysis is discussed in

[18]. The main contributions of this work have some salient features, which are highlighted as follows:

- i. The LLAD algorithm has extraction capabilities of fundamental current without prior knowledge of grid voltages. Therefore, this algorithm becomes reliable and invulnerable during abnormal voltage conditions.
- ii. The amplitudes of fundamental component of load currents are independently extracted for different three phases by LLAD algorithm. Therefore, it is not affected while extracting amplitude of fundamental component of other phases $u_{pc} = (v_{sc}/V_t)$.
- iii. The reactive power demanded by load side network is provided by PV coupled voltage source converter (VSC) to make unity power factor (UPF) in source side network. The UPF operation of system is demonstrated by experimental results in real-time implementation.
- iv. To make robust performance of the system even under dynamic conditions such as variable insolation, frequently varying local loads a feed-forward term is introduced to make fast dynamic response and stable during disturbance in the system.
- v. The proposed LLAD-based control algorithm is assured convergence during abnormal grid conditions such as distorted grid voltage, voltage sag and voltage swell.

To validate the performance of the presented system, the design, modelling and simulation of proposed system, are carried out in MATLAB®/Simulink environment. To validate the control algorithm, experimental results are obtained on a developed prototype for various operating conditions.

2 System configuration

The proposed system consists of a three phase grid, a ripple filter, a solar PV array, interfacing inductors, VSC and DC-link capacitor. Fig. 1a shows the configuration of proposed system. It is modelled and its behaviour is simulated for three-phase grid connected with a PV array having the loads which are connected at the point of common coupling (PCC). The design, modelling and selection procedures are given in [12, 13, 19].

3 Control algorithm

Fig. 1b shows overall structure of control algorithm for VSC switching operations to meet the desired power quality improvement in the distribution network. The control algorithm includes two main algorithms: MPPT algorithm and VSC switching algorithm. A perturb and observe (P&O)-based MPPT algorithm is used to generate reference voltage for regulation of DC-link voltage. The flowchart of the P&O algorithm is given in Fig. 1c.

3.1 VSC switching algorithm

Fig. 1b shows LLAD-based control algorithm to estimated reference grid currents, which proceeds further to generate switching pulses for VSC. The VSC switching algorithm is divided into small subsections such as evaluation of unit templates, feed-forward term, active and reactive loss components and amplitude of fundamental load components, estimation of reference grid currents, generation of pulse width modulation (PWM) pulses for insulated-gate bipolar transistor switching of VSC via PWM controller.

3.1.1 Estimation of amplitude of terminal voltage: The amplitude of PCC voltage is estimated from phase voltages. The sensed line voltages are passed through band pass filter having lower cut-off frequency of $\omega_{lower} = 2*\pi*48$ rad/s and higher cut-off frequency of $\omega_{upper} = 2*\pi*52$ rad/s. Using two sensed line voltages (v_{sab}, v_{sbc}), the phase voltages are estimated. The phase voltages (v_{sa}, v_{sb}, v_{sc}) are estimated as [19]

$$\begin{bmatrix} v_{sa} \\ v_{sb} \\ v_{sc} \end{bmatrix} = \frac{1}{3} \begin{bmatrix} 2 & 1 \\ -1 & 1 \\ -1 & -2 \end{bmatrix} \begin{bmatrix} v_{sab} \\ v_{sbc} \end{bmatrix} \quad (1)$$

After estimating phase voltages, the amplitude of terminal voltage (V_t) is estimated as

$$V_t = \sqrt{\frac{2}{3}(v_{sa}^2 + v_{sb}^2 + v_{sc}^2)} \quad (2)$$

3.1.2 Evaluation of in-phase and quadrature unit templates: The in-phase unit templates are computed by taking ratio of phase voltages (v_{sa}, v_{sb} and v_{sc}) and amplitude of terminal voltage for respective phases. The synchronising signals such as in-phase unit templates (u_{pa}, u_{qb} and u_{qc}) are evaluated as [19]

$$u_{pa} = \frac{v_{sa}}{V_t}, \quad u_{pb} = \frac{v_{sb}}{V_t}, \quad (3)$$

The quadrature templates which are 90° phase shifted from in-phase unit templates and these are evaluated from mathematical computation of in-phase unit templates. The synchronising signals such as quadrature unit templates (u_{qa} and u_{qb} and u_{qc}) are evaluated as [19]

$$\begin{aligned} u_{qa} &= -\frac{u_{pb}}{\sqrt{3}} + \frac{u_{pc}}{\sqrt{3}}, & u_{qb} &= \frac{\sqrt{3}u_{pa}}{2} + \frac{u_{pb} - u_{pc}}{2\sqrt{3}}, \\ u_{qc} &= -\frac{\sqrt{3}u_{pa}}{2} + \frac{u_{pb} - u_{pc}}{2\sqrt{3}} \end{aligned} \quad (4)$$

3.1.3 PV feed-forward component: In practical scenario of grid tied PV system, disturbances occur due to continuous variation of loads and atmospheric conditions. The feed-forward term is required to facilitate in the control algorithm in order to provide fast dynamic response. The PV feed-forward component is estimated from power of PV array and amplitude of terminal voltage. The feed-forward component is used to reduce oscillation in grid currents. The PV feed-forward component (w_{pv}) is estimated as

$$w_{pv} = \frac{2P_{pv}}{3V_t} \quad (5)$$

The adjustments in grid currents are required during variation in PCC voltages. This requirement is handled by PV feed-forward term. Moreover, to incorporate the changes in environmental conditions on PV power (P_{pv}), these are accommodated via PV feed-forward term into active power component.

3.1.4 Estimation of active and reactive loss components: The DC-link voltage is adaptively maintained to reference voltage to minimise the converter losses and also to avoid tripping of converter under weak grid conditions. To ensure the regulation in DC-link voltage as per desired value, a proportional integral (PI) controller is used. The error in-between sensed voltage at PCC and amplitude of terminal voltage is passed through a PI controller. The instantaneous error of amplitude of PCC voltage ($V_{te}(n)$) at n th sampled is given as

$$V_{te}(n) = V_m(n) - V_t(n) \quad (6)$$

The reactive loss component available at output of PI controller is used to regulate the terminal voltage at PCC. The reactive loss component (w_{cq}) is estimated as

$$\begin{aligned} w_{cq}(n+1) &= w_{cq}(n) + K_{pr}(V_{te}(n+1) - V_{te}(n)) \\ &+ K_{it}(V_{te}(n)) \end{aligned} \quad (7)$$

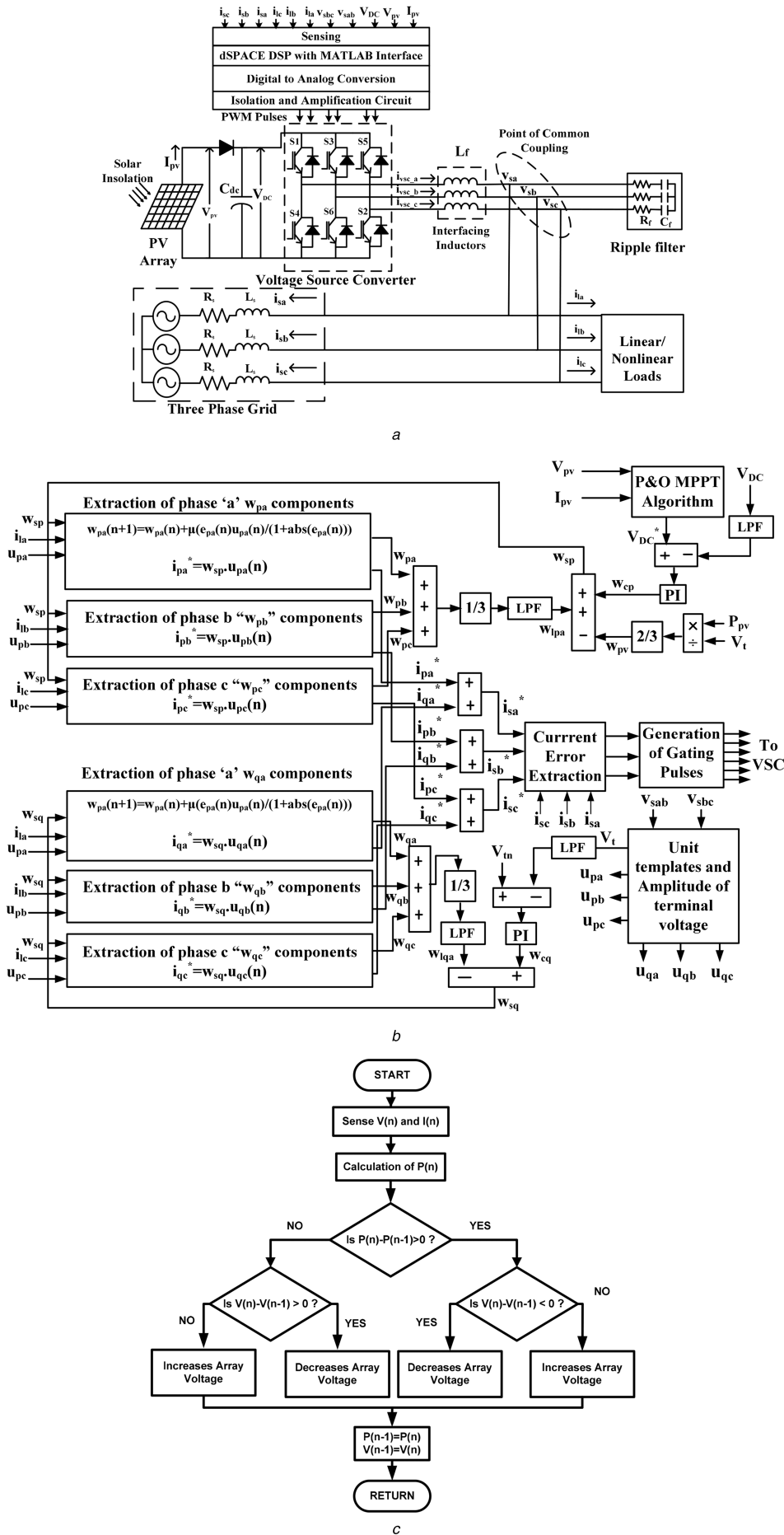


Fig. 1 Schematic diagram of topology and proposed control scheme

(a) Configuration of single-stage grid interfaced PV system, (b) Overall structure of LLAD-based control algorithm, (c) Flowchart of P&O-based MPPT algorithm

where K_{pi} and K_{it} are proportional and integral constants, which are used in the PI controller.

Similarly, the DC-link voltage error, which is evaluated from reference DC-link voltage and sensed DC-link voltage, is passed through a PI controller. The n th sampled instantaneous error of DC-link voltage ($V_{de}(n)$) is given as

$$V_{de}(n) = V_{DC}^*(n) - V_{DC}(n) \quad (8)$$

The active loss component is accessible at output of PI controller, which is opted to regulate DC link voltage. The active loss component (w_{cp}) is evaluated as

$$w_{cp}(n+1) = w_{cp}(n) + K_{pd}(V_{de}(n+1) - V_{de}(n)) + K_{id}(V_{de}(n+1)) \quad (9)$$

where K_{pd} and K_{id} are proportional and integral constants, which are used in the PI controller.

3.1.5 Extraction of weight of fundamental active and reactive component of load currents: The logarithmic absolute-based control algorithm has advantage of higher and lower amount of errors, which are into single adaption algorithm. For small perturbation of error, small steady-state means square error is achieved via higher order optimisation technique. Therefore, LLAD algorithm provides comparable convergence rate as compared to conventional algorithm. The active weight of the fundamental load component of phase 'a' is estimated as

$$w_{pa}(n+1) = w_{pa}(n) + \mu \times \frac{e_{pa}(n) \times u_{pa}(n)}{1 + |e(n)|} \quad (10)$$

where $e_{pa}(n)$ is error of adaptive integrant, which is estimated from load current of phase 'a', active weight of load component and in-phase unit template. The error for phase 'a' is estimated as

$$e_{pa}(n) = i_{ia}(n) - u_{pa}(n) \times w_{pa}(n) \quad (11)$$

Similarly, the weight of fundamental component for other two phases, are evaluated as

$$w_{pb}(n+1) = w_{pb}(n) + \mu \times \frac{e_{pb}(n) \times u_{pb}(n)}{1 + |e(n)|} \quad (12)$$

$$w_{pc}(n+1) = w_{pc}(n) + \mu \times \frac{e_{pc}(n) \times u_{pc}(n)}{1 + |e(n)|} \quad (13)$$

The reactive weight of the fundamental load component for phase 'a' is estimated as

$$w_{qa}(n+1) = w_{qa}(n) + \mu \times \frac{e_{qa}(n) \times u_{qa}(n)}{1 + |e(n)|} \quad (14)$$

where $e_{qa}(n)$ is error of adaptive integrant, which is estimated from load current of phase 'a', reactive weight of load component and quadrature unit template. The error for phase 'a' is evaluated as

$$e_{qa}(n) = i_{ia}(n) - u_{qa}(n) \times w_{qa}(n) \quad (15)$$

Similarly, the weight of fundamental reactive component for other two phases, are evaluated as

$$w_{qb}(n+1) = w_{qb}(n) + \mu \times \frac{e_{qb}(n) \times u_{qb}(n)}{1 + |e(n)|} \quad (16)$$

$$w_{qc}(n+1) = w_{qc}(n) + \mu \times \frac{e_{qc}(n) \times u_{qc}(n)}{1 + |e(n)|} \quad (17)$$

3.1.6 Estimation of reference grid currents: The net weight of active component of reference grid currents is evaluated by adding

average fundamental active weight component to DC loss component and by subtracting the PV feed-forward component

$$w_{sp} = w_{lpa} + w_{cp} - w_{pv} \quad (18)$$

where $w_{lpa} = (w_{pa} + w_{pb} + w_{pc})/3$.

The reference active component of grid currents are estimated as

$$i_{pa}^* = w_{sp} \cdot u_{pa}, \quad i_{pb}^* = w_{sp} \cdot u_{pb}, \quad i_{pc}^* = w_{sp} \cdot u_{pc} \quad (19)$$

The total weight of reactive component of reference three-phase grid currents is estimated by subtracting average reactive weight of fundamental component to AC loss component

$$w_{sq} = w_{cq} - w_{lqa} \quad (20)$$

where $w_{lqa} = (w_{qa} + w_{qb} + w_{qc})/3$.

The reference reactive component of grid currents is estimated as

$$i_{qa}^* = w_{sq} \cdot u_{qa}, \quad i_{qb}^* = w_{sq} \cdot u_{qb}, \quad i_{qc}^* = w_{sq} \cdot u_{qc} \quad (21)$$

Hence, reference grid currents are estimated as

$$i_{sa}^* = i_{pa}^* + i_{qa}^*, \quad i_{sb}^* = i_{pb}^* + i_{qb}^*, \quad i_{sc}^* = i_{pc}^* + i_{qc}^* \quad (22)$$

The switching signals of VSC are generated by indirect current control with the hysteresis controller. The input of hysteresis controller having width of $\delta=0.02$ is error between three phase reference currents (i_{sa}^* , i_{sb}^* and i_{sc}^*) and sensed three-phase grid currents (i_{sa} , i_{sb} and i_{sc}).

3.2 Procedure to obtain μ value

The value of μ is chosen in a way that it does not transgress the bound given in [18]. For different values of μ (0.09, 0.016 and 0.05), MSD graphs are shown in Figs. 2a–c. The performance of the system for different value of μ is demonstrated in Figs. 2a–c. Figs. 2a–c show the MSD of the algorithm for $\mu=0.009$, 0.016 and 0.05, respectively. Fig. 2b shows that the algorithm (with $\mu=0.016$) has superior performance to track the amplitude of the fundamental load component as compared to other different values of μ (0.009 and 0.05). In the proposed scheme, the MSD value is more negative implying least error as desired.

4 MATLAB modelling and simulation performance

The single-stage three-phase grid interfaced PV system using LLAD control algorithm is modelled and its performance is simulated in MATLAB[®]/Simulink using Simscape toolbox. The comprehensive system parameters are given in Table 1. The performance of presented system is subjected to various test conditions such as steady state, variable insolation and load unbalancing for analysing the performance of the system. To analyse dynamics of presented system, simulated results involve significant signals such as grid voltages and currents (v_{sabc} , i_{sabc}), load current of phase 'a' (i_{la}), VSC currents (i_{vsc}), power of PV array (P_{pv}), PV array voltage and current (V_{pv} , I_{pv}), DC-link voltage (V_{DC}), PV array power (P_{pv}), peak of component of fundamental load current of phase 'a' (w_{ap}), feed-forward component (w_{pv}), active loss component (w_{cp}), active power (P_s) and reactive power (Q_s) of grid, which are well demonstrated here for different operating conditions.

4.1 Dynamic performance under non-linear load

Fig. 3a illustrates dynamic in V_{DC} , I_{pv} , V_{pv} , P_{pv} , w_{pa} , w_{pv} , w_{sp} . The DC-link voltage is maintained stable and regulated according to MPPT algorithm even under unbalancing to balancing in the load side network. The solar PV array current and solar PV array power

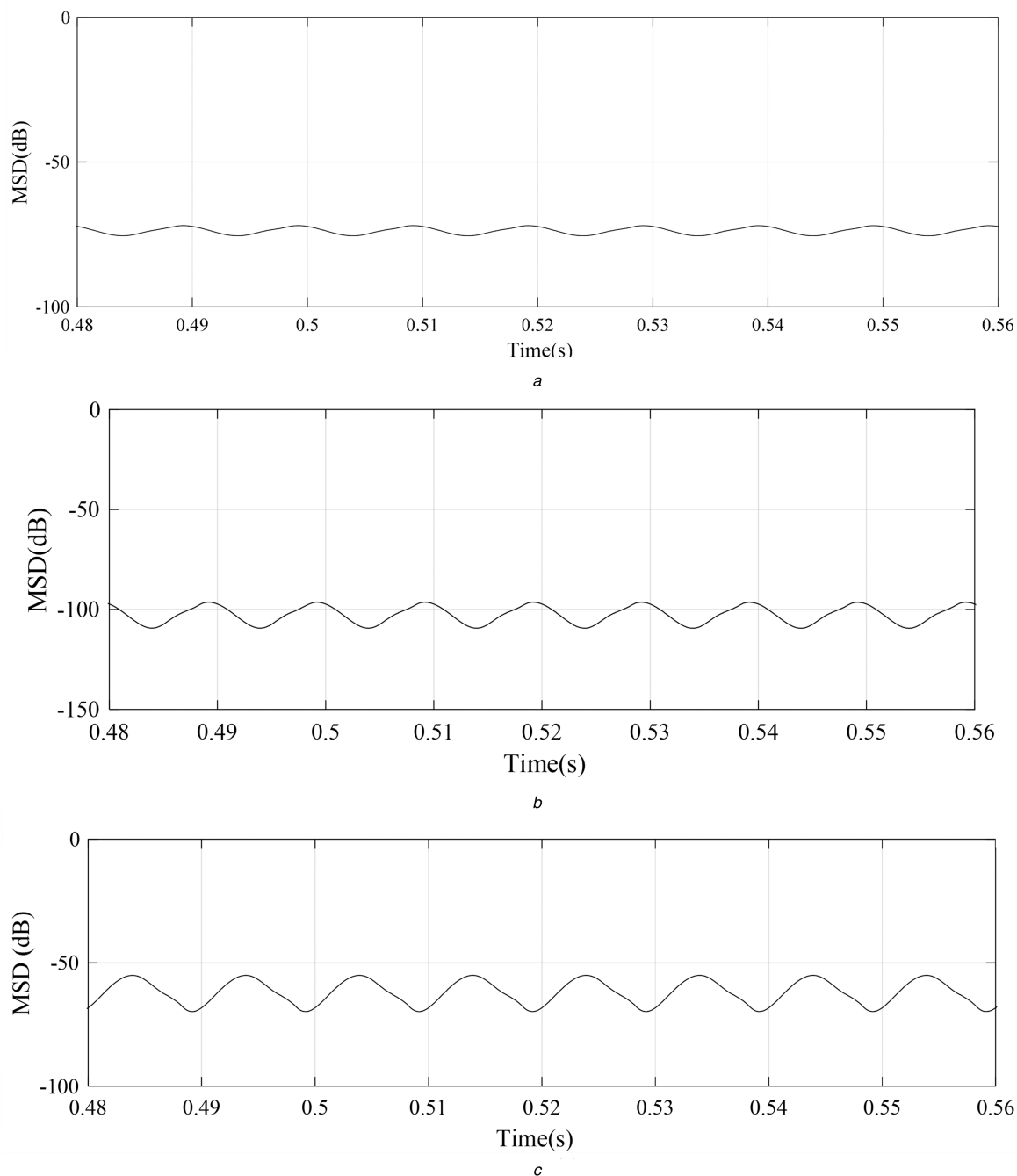


Fig. 2 Performance of the algorithm for different μ values
(a) 0.009, (b) 0.016, (c) 0.05

Table 1 Simulated system parameters

Parameter	Value	Parameter	Value
PV module short circuit current	$I_{sc} = 8.21$ A	DC-link capacitor	$C_{DC} = 6500$ μ F
PV module open circuit voltage	$V_{oc} = 32.9$ V	interfacing inductor	$L_f = 2.5$ mH
PV array power	$P_{pv} = 5.35$ kW	grid voltage	$v_{sab} = 218$ V
AC PI Controller	$K_{pd} = 0.8, K_{pi} = 0.2$	DC-link voltage, V_{DC}	$V_{DC} = 340$ V
DC PI controller	$K_{pd} = 9, K_{id} = 40$	ripple filter	$R_{f,,} = 5$ $\Omega, C_f = 10$ μ F
μ	0.016	nonlinear load	$R_L = 50$ $\Omega, L = 100$ m H
T_s	30 μ s	rating of grid	$(X/R)_{weak} < 3; (X/R)_{stiff} > 10,$

remain unaffected as depicted in Fig. 3a. The weight of load component is increased as the load is balanced in load side network. The PV feed-forward component remains unaffected under load unbalancing to load balancing. The net weight of current component is decreased, which results into increment in amplitude of the reference grid currents as depicted in Fig. 3b.

Fig. 3b shows dynamic of $v_{sabc}, i_{sabc}, i_{ref}, i_{labc}, P_s,$ and Q_s . The grid currents are balanced and sinusoidal even under dynamic operating condition. The grid currents are successfully tracking the reference grid currents as depicted in Fig. 3b. The load power requirement is decreased due to load balancing to load unbalancing. The load power is decreased and the grid current is increased, which is

demonstrated by noticeable change in power flow in the grid as shown in Fig. 3b. The reactive power flow in the distribution network is null, which demonstrates the UPF operation of the distribution network in Fig. 3b. The total harmonic distortions (THDs) of grid currents remain within limits of IEEE-519 standard [20].

4.2 System performance under variable insolation condition

Figs. 3c and d illustrate performance of the system under linear load by decreasing solar insolation from 1000 to 700 W/m² at 0.5 s. Fig. 3c shows the dynamics in insolation, G , V_{DC} , I_{pv} , V_{pv} , P_{pv} , w_{pa} , w_{pv} , w_{sp} . The DC-link voltage is maintained stable under variation of solar insolation from 1000 to 700 W/m² as shown in Fig. 3c. The solar PV array current and power are decreased as solar insolation decreased as shown in Fig. 3c. The active weight of the fundamental load component remains unchanged under variation of solar power generation. The feed-forward component is decreased as solar insolation level is decreased from 1000 to 700 W/m². The net active weight of load component is decreased as PV feed-forward component is decreased as shown in Fig. 3c.

Fig. 3d illustrates the dynamic of v_{sabc} , i_{sabc} , i_{ref} , i_{labc} , P_s , and Q_s . As the solar insolation is decreased, the power generation by PV array is decreased and that is reflected by decreasing PV array power and PV-VSC currents. The load power is constant during this operation. Feeding of active power to the grid is also decreased, which is demonstrated by the grid power as it becomes less negative and a small decrement in grid currents. The reactive power flow in the distribution network is null, which demonstrates the UPF operation of the distribution network in Fig. 3d. The dynamics of system looks smooth and controlled even though sudden change in insolation due to existence of feed-forward term.

4.3 Comparative analysis between conventional algorithms and presented LLAD algorithm

Fig. 4 demonstrates the comparative performance of presented LLAD algorithm with the conventional LMF algorithm. Simulation results have been presented for LLAD and LMF algorithms. In steady-state condition, the oscillations are also less in w_{pa} as compared to conventional LMF algorithm, which is illustrated in Fig. 4. The LMF algorithm has taken more time to converge to estimate amplitude under load unbalancing. The reason behind slow convergence is explained as follows. The error in LMF algorithm has been cubed, when the error between the load current and the estimated value is very less, lesser than unity, the weights of the algorithm take too long time to converge to the actual value under perturbations in load. When the phase a load is disconnected, due to the error being greater than unity, the weight of LMF algorithm, immediately starts converging in a quick manner till the time error reaches unity. As soon as the, error reaches unity, the weight update of LMF algorithm becomes drastically slow.

To demonstrate importance of PV feed-forward term into control scheme, the behaviour of the system with and without feed-forward term is illustrated under non-linear load in Figs. 5a–d as solar power generation is decreased. Figs. 5a and b show the performance of the grid interfaced solar PV with the PV feed-forward component. Fig. 5a shows dynamics in G , V_{DC} , I_{pv} , P_{pv} . There are no oscillations in DC-link voltage even under variation of solar power generation. As the insolation decreases, solar PV array current and power are decreased, which result into noticeable decrement in magnitude of grid currents. Fig. 5b shows waveforms of v_{sabc} , i_{sabc} , i_{labc} and i_{vsc} . Due to decrement in solar power generation, the power flow in the grid is decreased, which is demonstrated by noticeable change in grid currents under fixed load power shown in Fig. 5b. There are no oscillations observed in grid currents due to accounting PV feed-forward component into control scheme. Figs. 5c and d have illustrated the dynamics of the system without considering PV feed-forward term into control algorithm. Fig. 5c shows waveforms of G , V_{DC} , I_{pv} , P_{pv} . Due to not accounting of PV feed-forward term in control scheme, oscillations are observed in DC bus voltage as solar power generation varies.

Fig. 5d shows waveforms of v_{sabc} , i_{sabc} , i_{la} and i_{vsc} . There are noticeable oscillations in grid currents as solar power generation is varied due to variation in solar insolation.

Table 2 provides comparative evolution and analysis amongst various conventional algorithms such as LMF and SRF. The comparison of THDs of grid currents of conventional algorithm with presented algorithm is shown in Table 3. The THDs of grid currents are 3.2 and 4% for LLAD and LMF algorithm, respectively. From Tables 2 and 3, it is easy to understand that the LLAD algorithm is less complex, requires less computations, high digital signal processing (DSP) speed, low THDs, less settling time.

5 Hardware implementation

A prototype of single-stage, three-phase grid interfaced PV system is developed in the laboratory for substantiation of the control and also analysed in the MATLAB[®]/Simulink. A solar PV array simulator (AMTEK make ETS600/17DPVF) having capacity of 5.35 kW is utilised for practical implementation of solar power generating system. The grid voltages and PV voltage are sensed by Hall Effect voltage sensors (LV25-P). The load currents, inverter output currents, grid currents and PV array current are sensed by Hall Effect current sensors (LA55-P). To provide isolation between VSC and digital signal processor, opto-couplers are used. The LLAD-based control algorithm is implemented through a digital signal processor (dSPACE-1202, MicroLabBox). To analyse the performance of grid connected PV array, power analyser (Fluke-43B), high-resolution power analyser (Yokogawa-WT1800) and digital storage oscilloscope (Agilent-DSO0614A) are utilised. The comprehensive data for hardware implementation is given in Table 4.

5.1 Steady-state behaviour of system under non-linear load

Figs. 6 and 7 demonstrate the performance of the system under a non-linear load of 1.49 kVA. Figs. 6a–c illustrate the voltage and current waveforms of grid, load and PV-VSC. The voltage and current waveforms of grid are out of phase, which illustrates that the power is fed into the grid. Figs. 6d and 7a and b illustrate the power flow in grid, power consumption by load and power supplied by PV coupled VSC. The power of grid, load and PV-VSC are 3.53 kW, 1.49 and 5.05 kW, respectively. The PV coupled VSC feeds power to the load and surplus power to the grid, which is also demonstrated by sum of grid and load power, is equivalent to the power of solar PV coupled VSC.

However, Fig. 7c demonstrates that THD of grid current is 2.9%, which is found within limit of an IEEE-519 standard [20]. Owing to non-linear load at PCC, Fig. 7d shows that the THD of load current is 26.9%, which is responsible for deterioration in the power quality of the distribution network. Moreover, non-linear load demands harmonics, which are supplied by PV-VSC at PCC. The losses in VSC are 300 W (5.35–5.05 = 300 W). Therefore, efficiency of PV-based system is 94.69%. The experimental results demonstrate that efficiency of single-stage system is higher than double-stage system topology, which is reported in [15].

5.2 Performance of system under variable solar insolation

Figs. 8a–d show MPPT performance and dynamic response of the system under time varying solar insolation condition. Figs. 8a–b show MPPT performance of PV simulator at insolation decreased from 1000 and 700 W/m² with 100% efficiency. The voltage and current (V_{mpp} and I_{mpp}) of maximum power point at insolation level 1000 and 700 W/m² are marked in Figs. 8a–b. Figs. 8c–d show dynamics of DC-link voltage, PV array, PV-VSC current and grid current of phase ' i ' which are analysed in Fig. 8c. The DC-link voltage is regulated balanced and stable according to MPPT algorithm. As solar insolation is decreased from 1000 to 700 W/m², PV array current is decreased. Moreover, the load currents remain unaffected so that there is no variation in power consumption in the load side network. Hence, power flow in the grid is decreased as the solar power generation is decreased.

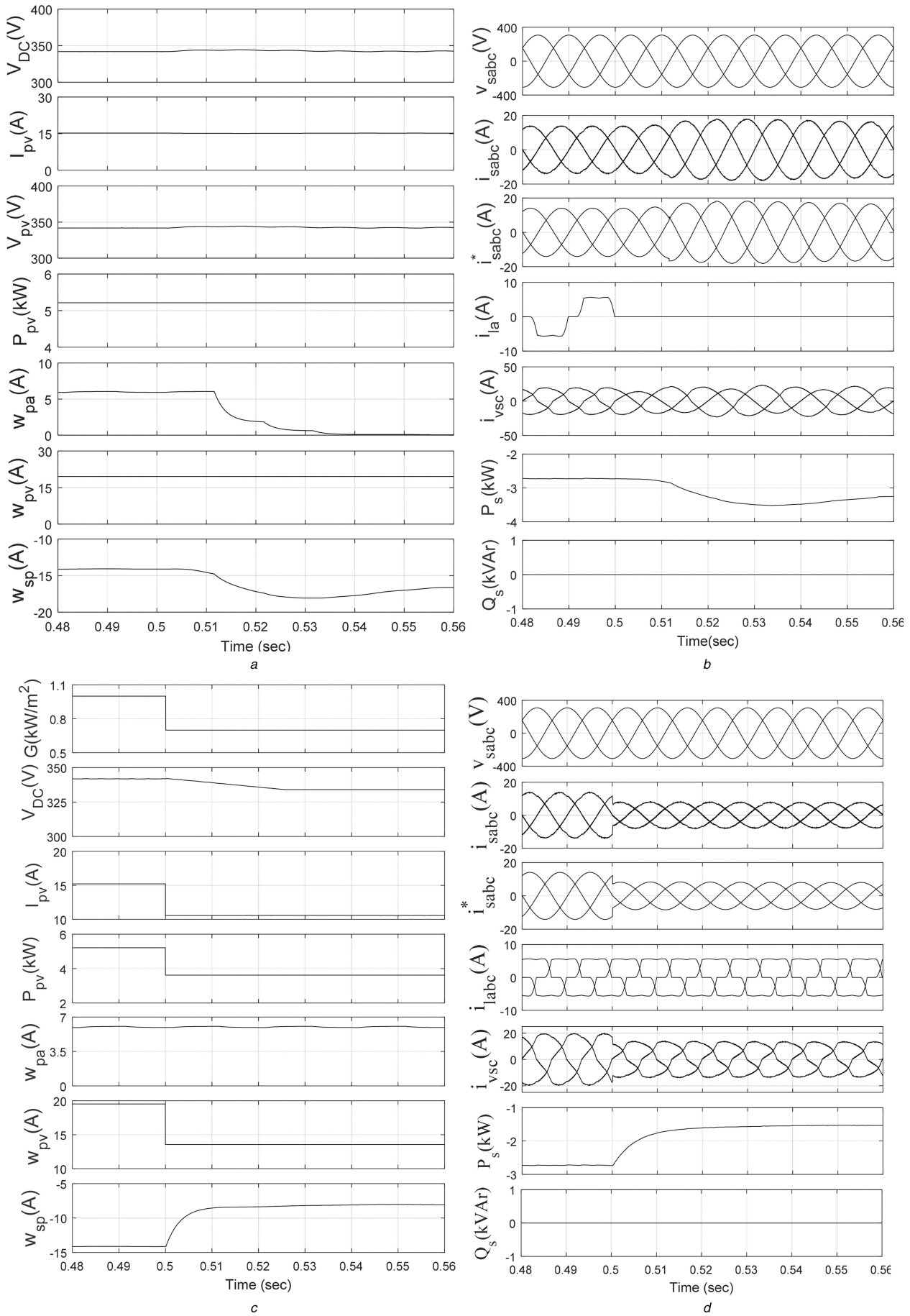


Fig. 3 Dynamics of system under unbalancing load side network and variable solar insolation

(a) V_{DC} , I_{pv} , V_{pv} , P_{pv} , w_{pa} , w_{pv} , w_{sp} , (b) v_{sabc} , i_{sabc} , i_{ref} , i_{la} , P_s , and Q_s , (c) G , V_{DC} , I_{pv} , P_{pv} , w_{pa} , w_{pv} , w_{sp} , (d) v_{sabc} , i_{sabc} , i_{ref} , i_{labc} , P_s , and Q_s

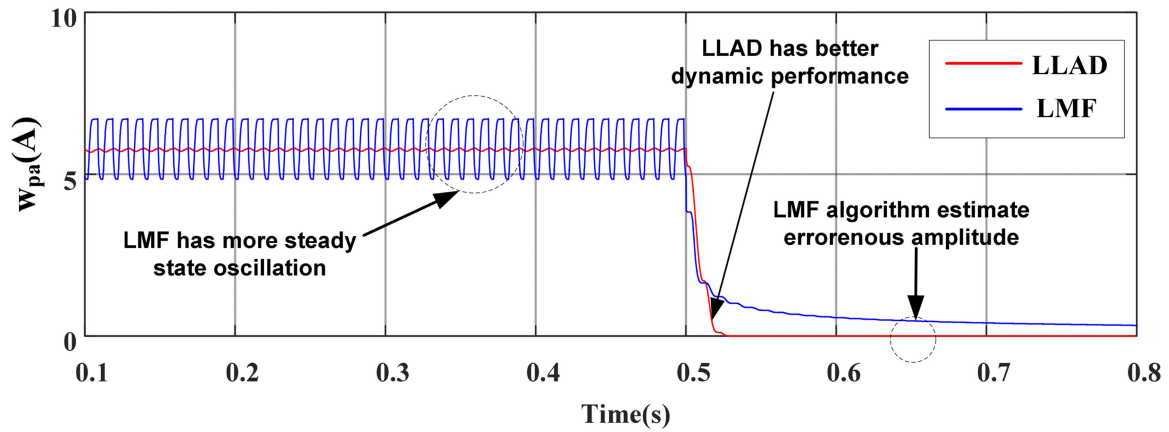


Fig. 4 Comparative performance LLAD algorithm with conventional LMF algorithm

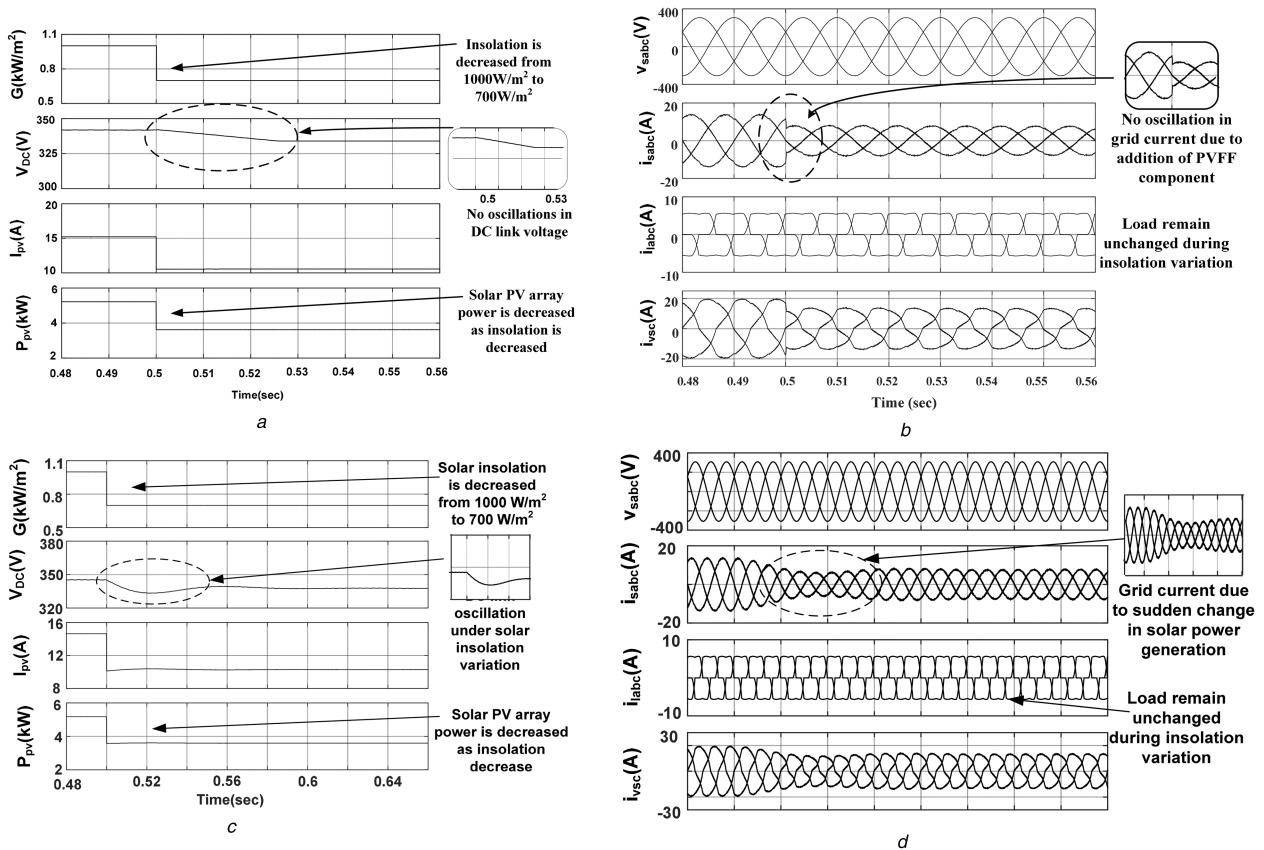


Fig. 5 Effect of PV feed-forward term into control scheme (a) $G, V_{DC}, I_{pv}, P_{pv}$, (b) $v_{sabc}, i_{sabc}, i_{labc}, i_{vsc}$, (c) $G, V_{DC}, I_{pv}, P_{pv}$, (d) $v_{sabc}, i_{sabc}, i_{labc}, i_{vsc}$

Table 2 Comparative analysis between various algorithms

Parameters	LLAD	LMF	SRFT
type of filter	adaptive filter	adaptive filter	time-domain PLL
accuracy	Better	poor	good
oscillations in amplitude estimation	0.1 A	2.5 A	0.3 A
complexity	low	low	high
computational burden	0.4 ms	0.39 ms	3.8 ms
no. of computation	low	low	high
DSP speed	more	more	less
memory requirement	low	low	relatively high
sampling time	30 μ s	30 μ s	50 μ s

Therefore, the power contributed by PV-VSC to the grid is decreased, which is demonstrated by a decrement in PV-VSC current as well as the grid current of phase 'a'. Fig. 8d shows dynamics of active loss LMF component, feed-forward term, weight of

fundamental load current of phase 'a' and net active weight component. The loss component remains unaffected under variation of solar power generation. The active weight of fundamental load component is consistently tracked by LLAD

Table 3 THD report of system under nonlinear load

Operation	Name of waveform	Performance LLAD	Indices LMF
UPF	grid voltage, V, %THD	308 V, 0.18%	308 V, 0.18%
	grid current, A, %THD	14 A, 3.2%	14.12 A, 4%
	VSC current, A, %THD	19.8 A, 12.8%	19.91 A, 13.2%
	load current, A, %THD	5.8 A, 26.29%	5.8 A, 26.29%
	DC bus voltage, V	340 V	340 V

Table 4 Experimental parameters

Parameter	Value	Parameter	Value
PV module current at MPPT	$I_{mpp} = 15.75$ A	DC-link capacitor	$C_{DC} = 6500$ μ F
PV module voltage at MPPT	$V_{mpp} = 340$ V	interfacing inductor	$L_f = 2.5$ mH
PV array power	$P_{pv} = 5.35$ kW	grid voltage	$v_{sab} = 218$ V
μ	0.016	DC-link voltage V_{DC}	$V_{DC} = 283$ V
AC PI Controller	$K_{pd} = 0.1, K_{pi} = 0.02$	DC PI controller	$K_{pd} = 0.1, K_{id} = 0.0001$
nonlinear load	953 VA	ripple filter	$R_f = 5 \Omega, C_f = 10 \mu$ F
T_s	30 μ s	VSC rating	25 kVA

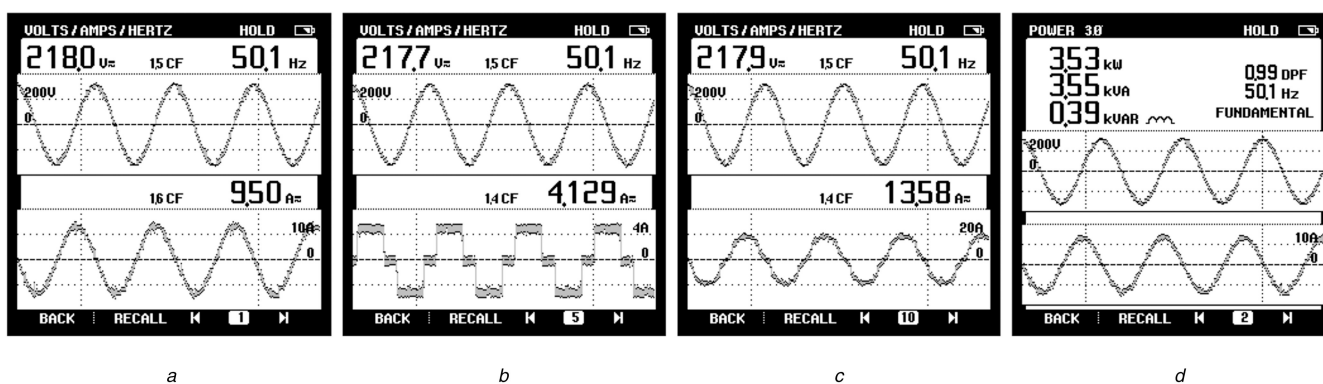


Fig. 6 Steady-state performance of the system under non-linear load (a-c) Voltage and current waveforms of grid, load and PV-VSC, (d) Grid power, P_{grid}

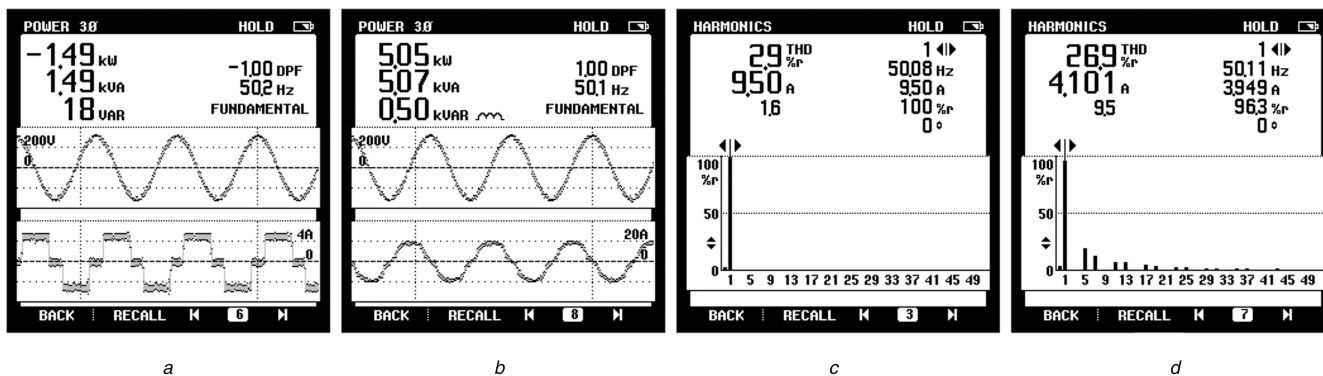


Fig. 7 Steady-state performance of the system under non-linear load (a-c) Load power and VSC power, P_{load}, P_{pv-vsc} , (d) THD of i_{sa}, i_a

algorithm even under variation of solar insolation as depicted in Fig. 8d. As solar insolation is decreased, feed-forward component is decreased and net weight is increased, which is illustrated in Fig. 8d.

5.3 Dynamic performance of system under unbalancing in load side network

Figs. 9a-d show the dynamics of system under balancing to unbalancing of phase 'a' of load side network. Figs. 9a and b show waveforms of line voltages (v_{sab} and v_{sbc}), phase voltages (v_{sa} , v_{sb} and v_{sc}) amplitude of terminal voltage (V_t), unit templates (u_{pa} and u_{pb}). The line voltages and unit templates are unaffected in spite of unbalancing in load side network. Hence, unit templates, which are

derived from line voltages, are unaffected under load unbalancing. Figs. 9c and d demonstrate the dynamics of phase 'a' during unbalancing in phase 'a' of load side network. Fig. 9c shows DC-link voltage, load current, PV-VSC current and grid current of phase 'a'. The DC-link voltage is maintained stable under the load balancing to unbalancing as shown in Fig. 9c. As the load balancing to unbalancing is occurred, the grid power is increased as demonstrated by noticeable increment in the grid current as depicted in Fig. 9c. The dynamics in phase 'a' of the solar PV coupled VSC system is demonstrated in Fig. 9c. Fig. 9d shows the dynamics of DC-link voltage, load current, PV-VSC current and grid current of phase 'b', which demonstrates the dynamics of phase 'b' when load unbalancing to balancing is occurred in phase 'a'. The grid current in phase 'b' is increased as the load is

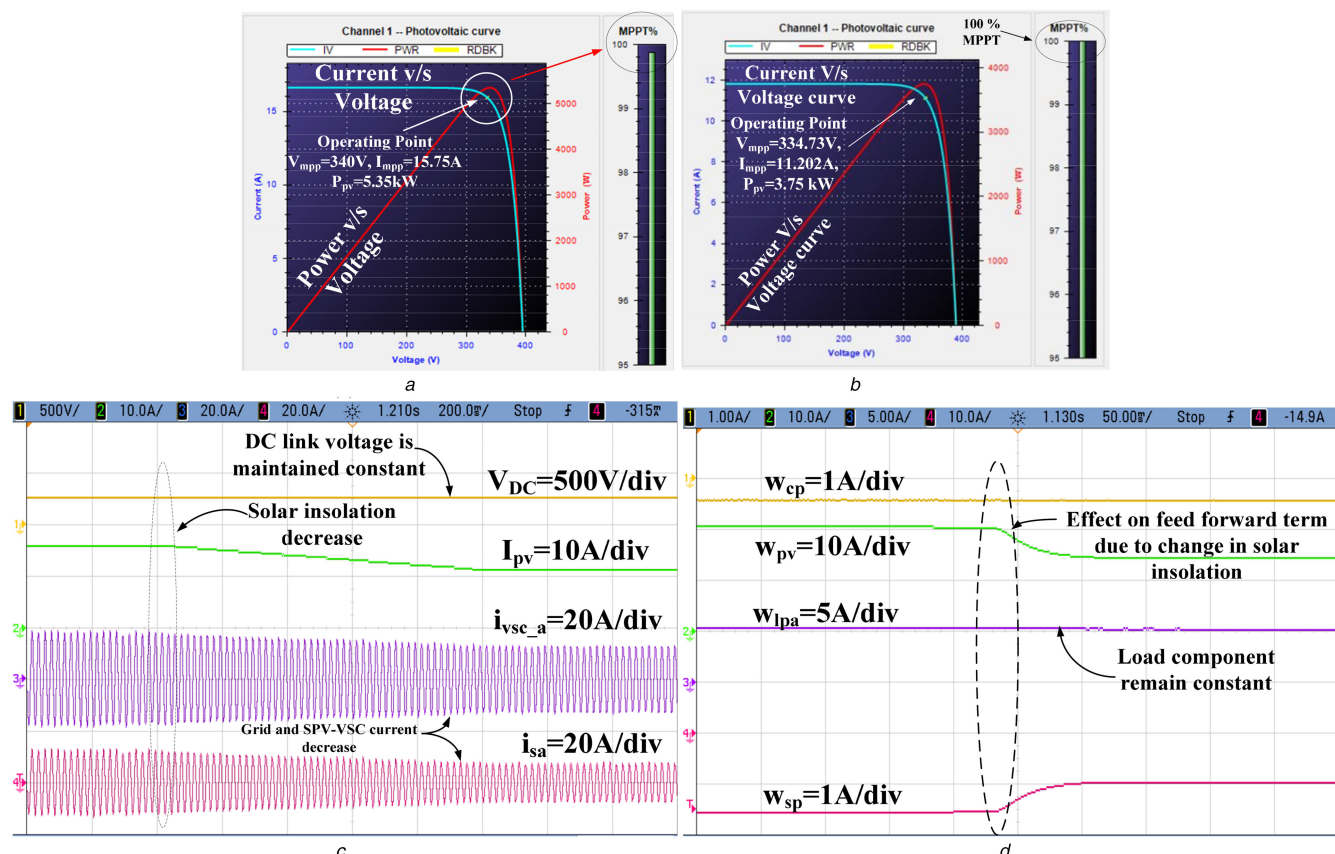


Fig. 8 Dynamic performance of the system under varying insolation from 1000 to 700 W/m²
 (a, b) MPPT performance of PV simulator V_{DC} , i_{pv} , i_{vsc_a} , i_{sa} , (d) w_{cp} , w_{pv} , w_{lpa} , w_{sp}

unbalanced in the load side network. Fig. 10a illustrates loss component, feed-forward term, load component and net weight of current. The loss component is little deviated from its value due to regulation of DC-link voltage according to reference voltage, which is generated by MPPT algorithm. The feed-forward term remains unaffected in spite of unbalancing in the load. The net weight of load component is decreased due to unbalancing in load side network. Moreover, net weight of active component is increased due to decrement in the load component. Fig. 10b demonstrates the dynamics of load current, unit template, error and active weight of fundamental load component phase 'a'. As load balancing to unbalancing is occurred in the load side network, the weight of fundamental load current of phase 'a' and active load weight component are decreased as observed in Figs. 10a and b.

5.4 Performance of system under abnormal grid condition

Figs. 10c and d show the performance of the system under abnormal grid conditions such as voltage sag and voltage swell phenomena. The dynamics in waveforms of line voltage, grid current, load current and PV-VSC current of phase 'a' are analysed under voltage sag phenomena in Fig. 10c. Fig. 10c illustrates abnormal grid condition as voltage sag [21], line voltages are decreased from 218 to 196 V (10% decrease). The grid current is increased due to power consumption of the load is decreased. The active weight of fundamental load component is decreased as load current is decreased as shown in Fig. 10c. However, weights of fundamental load currents are extracted without acquaintance of any abnormalities in grid voltages. The LLD-based control algorithm works in the following ways. The net current component is increased as the load component is decreased, which results into increment in amplitude of the reference grid current. Therefore, noticeable change in the grid current is observed under voltage sag as shown in Fig. 10c. Moreover, it is reliable during such kind of abnormalities in the grid. The dynamics in waveforms of line voltage, grid current, load current and PV-VSC current of phase 'a' are analysed under voltage swell phenomenon in Fig. 10d.

Moreover, Fig. 10d shows abnormal grid condition as voltage swell, line voltages are increased from 218 to 240 V (10% increase). Therefore, grid currents are decreased which demonstrates power fed by PV-VSC into the grid remains constant as demonstrated in Fig. 10d. The grid current is decreased due to power consumption of the load is increased. The active weight of fundamental load component is increased as the load current is increased as shown in Fig. 10d. The LLD-based control algorithm works in the following ways. The net current component is decreased as the load component is increased, which results into decrement in amplitude of the reference grid current. Therefore, noticeable change in the grid current is observed under voltage swell as shown in Fig. 10d. Moreover, the grid currents are maintained well balanced and sinusoidal.

5.5 Performance of system under distorted grid condition

The non-linear loads are connected in the distribution network, which are responsible for distortion in the grid voltages under weak grid condition. Thereby, displacement power factor (DPF) of grid voltages is deteriorated. Figs. 11a–d demonstrate DPF and THDs of grid voltages and grid currents without and with connecting of PV-VSC at PCC. Figs. 11a and b shows the analysis of the grid voltage and grid current under highly nonlinear load connected at PCC. Fig. 11b shows the waveforms of the grid voltage and grid current without switching on solar PV coupled VSC. The DPF of grid is degraded due to distorted grid condition in the distribution network and nonlinear load in load side network. The THDs of PCC voltages are higher than 5%, which is depicted in Fig. 11a. Moreover, the THDs of grid currents are higher than 24%. Figs. 11c and d show the waveforms and analysis of the grid voltage and grid current after connecting solar PV coupled VSC at PCC. When the PV coupled VSC is connected at PCC, grid voltages and grid currents are found balanced and sinusoidal with improved DPF from 0.90 to almost unity as illustrated in Fig. 11c. Even though the distortion in grid voltage is higher than 5%, the weight extraction of fundamental load current is not affected. The

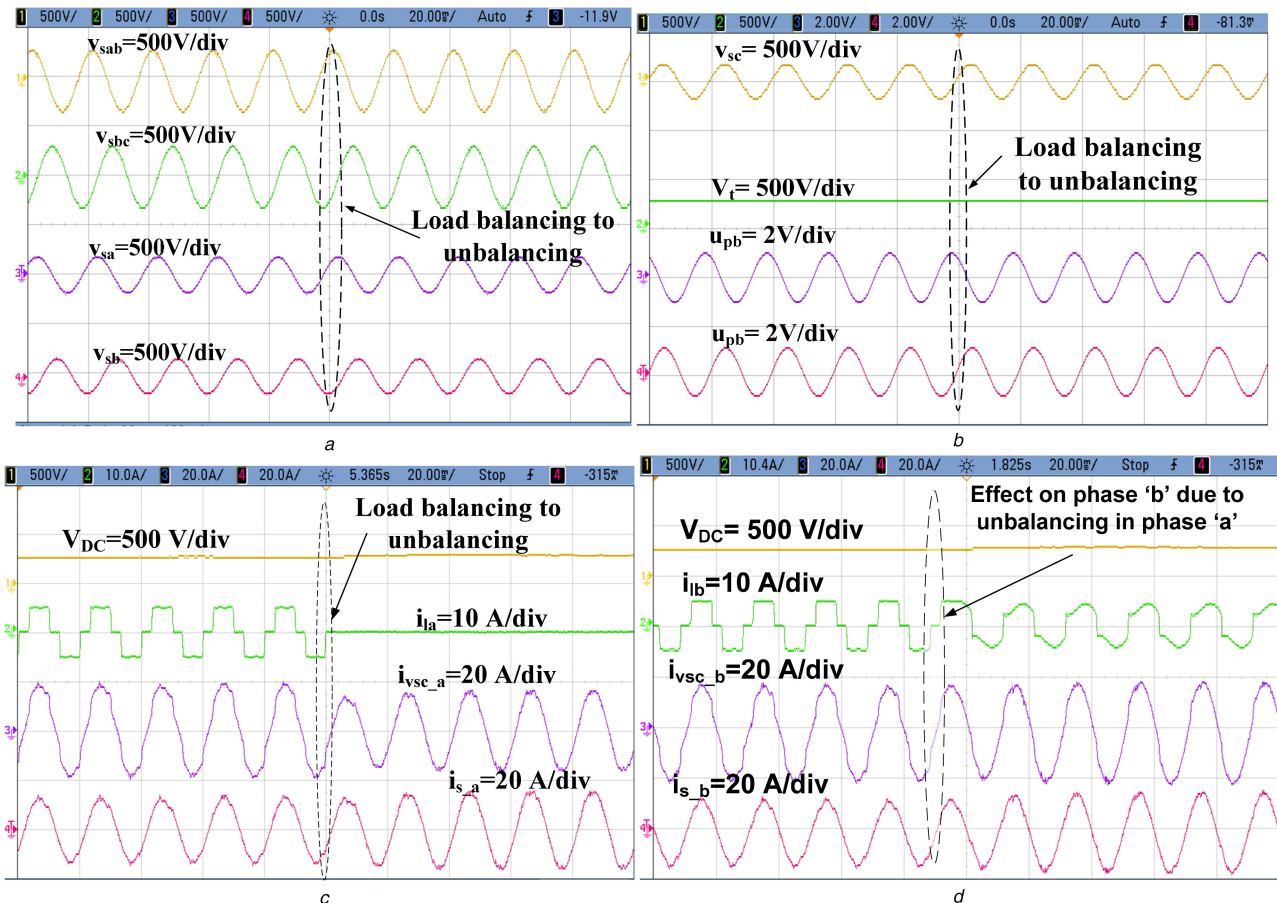


Fig. 9 Dynamics of system under unbalancing in load side network
 (a) v_{sab} , v_{sbc} , v_{sa} , v_{sb} , (b) v_{sc} , V_t , u_{pa} , u_{pb} , (c) V_{DC} , i_{la} , i_{vsc_a} , i_{sa} , (d) V_{DC} , i_{lb} , i_{vsc_b} , i_{sb}

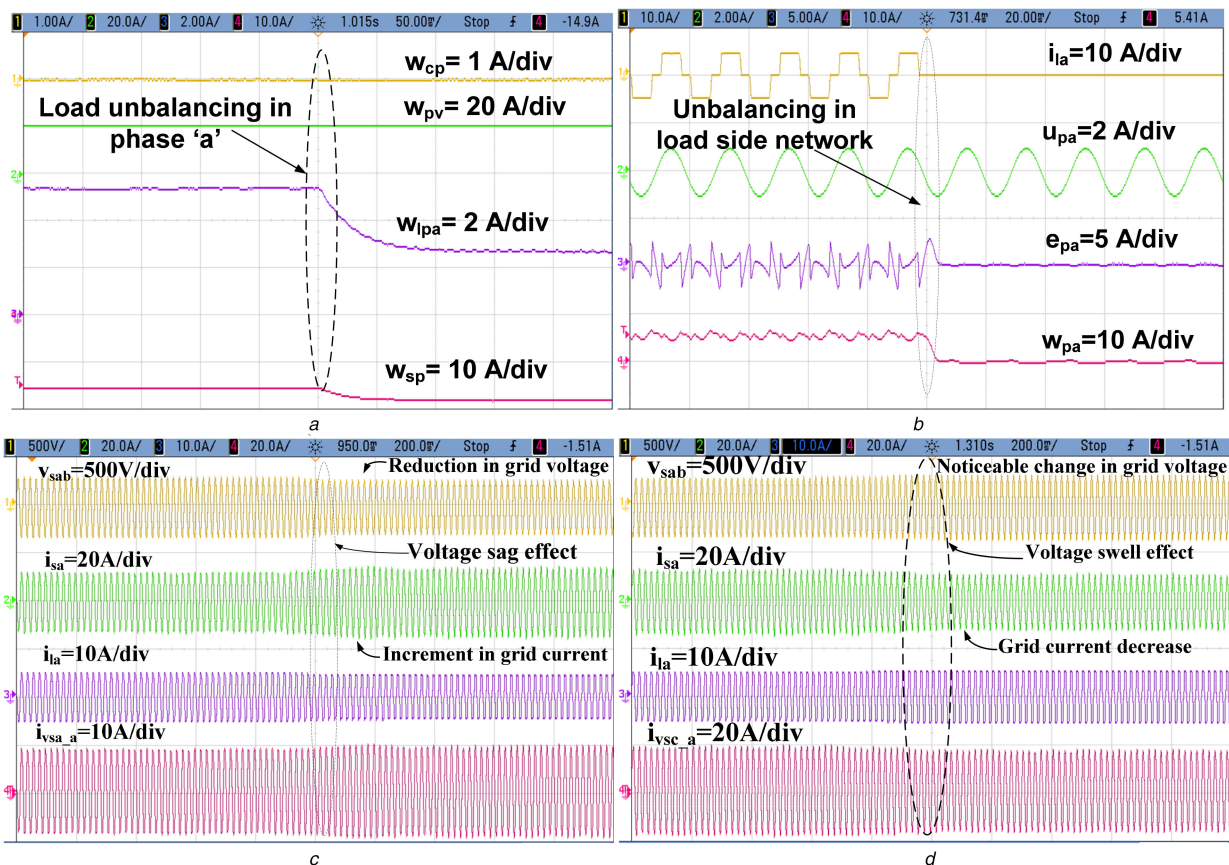


Fig. 10 Performance of system under unbalancing in load side network
 (a) w_{cp} , w_{pv} , w_{lpa} , w_{sp} , (b) i_{la} , u_{pa} , e_{pa} , w_{pa} , (c, d) Under abnormal condition in grid side network, (c) v_{sab} , i_{sa} , i_{la} , i_{vsc_a} , (d) v_{sab} , i_{sa} , i_{la} , i_{vsc_a}

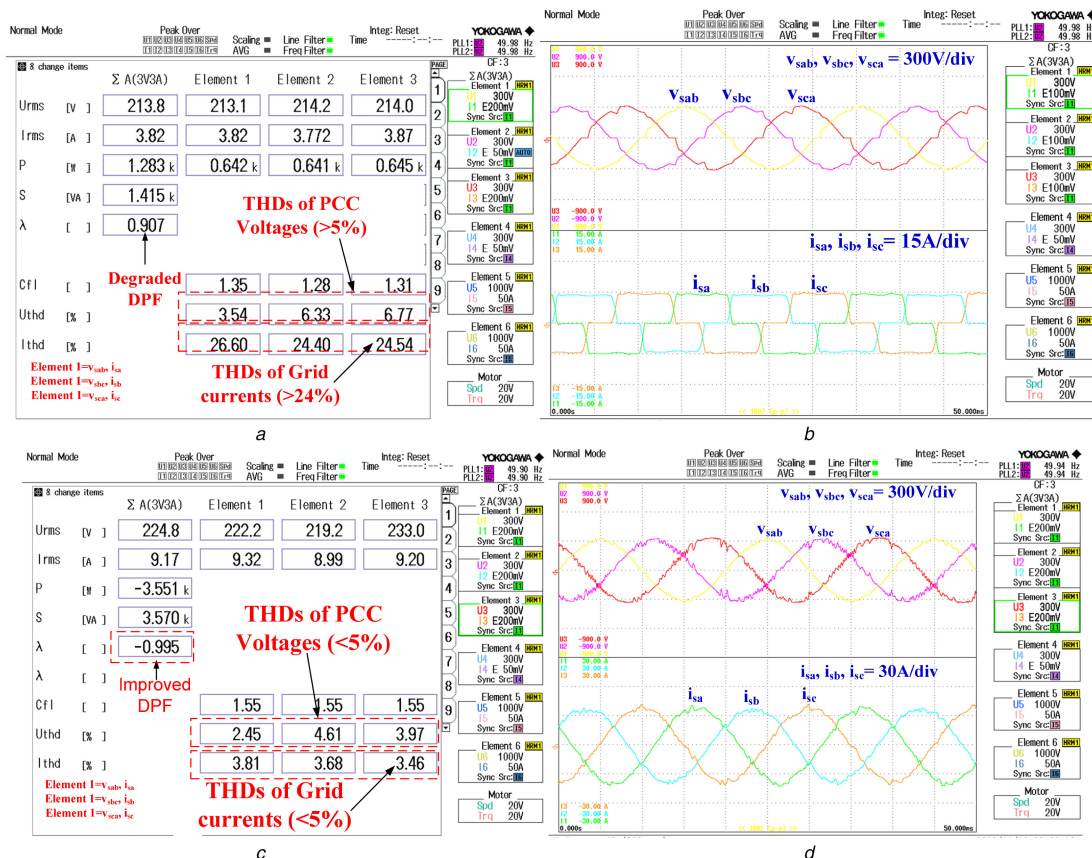


Fig. 11 Performance of system under distorted grid condition

(a) THDs of grid voltages and currents and source DPF before coupling PV-VSC at PCC, (b) Voltages and currents waveforms of the grid before connecting PV-VSC at PCC, (c) THDs of grid voltages and currents and source DPF after coupling PV-VSC at PCC, (d) Voltages and currents waveforms of the grid after connecting PV-VSC at PCC

DPF is improved due to harmonics requirement of load side network is supplied by PV coupled VSC at PCC. The THDs of grid voltage and grid currents are found <5%, which is well under limit of an IEEE-519 standard [20] as shown in Figs. 11c and d.

6 Conclusion

The fast and multifunctional control algorithm has been presented for single-stage three-phase grid tied PV system using LLAD adaptive filter with P&O-based MPPT algorithm. Simulated results have successfully demonstrated the reduced THDs of grid currents, load balancing, UPF operation even under non-linear load and varying insolation conditions. The comparative performance analysis between proposed and conventional control algorithms has been successfully demonstrated with manifold advantages. The control responses are reliable and it has enhanced the system performance in both steady-state and dynamics conditions. Moreover, test results have illustrated that by using single-stage topology, it has low losses and give rise to high efficiency in the VSC as compared to a double-stage grid interfaced system, which enhances the solar power penetration into the distribution network. Experimental results have shown that the power quality of the grid is improved under load unbalancing, variable insolation conditions and even under weak grid conditions such as voltages distortion, voltages sag. The THDs of grid currents and grid voltages are found <5% within limits of an IEEE-519 standard in a grid integrated renewable system.

7 Acknowledgments

The authors are highly thankful to DST, Govt. of India, for their financial support for this project under grant number: RP02979 (RESCUE-an Indo UK Project).

8 References

- [1] IEA: 'Transition to sustainable buildings: strategies and opportunities to 2050' (International Energy Agency (IEA), Paris, France, 2013)
- [2] Hsu, C.W.: 'Using a system dynamics model to assess the effects of capital subsidies and feed-in tariffs on solar PV installations', *Appl. Energy*, 2012, **100**, pp. 205–217
- [3] 'Solar rooftop-grid connected', Ministry of New and Renewable Energy (MNRE), Government of India. Available at <http://www.mnre.gov.in/schemes/decentralized-systems/solar-rooftop-grid-connected/>, accessed November 15 2016
- [4] Shongwe, S., Hanif, M.: 'Comparative analysis of different single-diode PV modeling methods', *IEEE J. Photovoltaics*, 2015, **5**, (3), pp. 938–946
- [5] Villalva, M.G., Gazoliand, J.R., Filho, E.R.: 'Comprehensive approach to modelling and simulation of photovoltaic arrays', *IEEE Trans. Power Electron.*, 2009, **24**, (5), pp. 1198–1208
- [6] Kaplani, E., Kaplansis, S.: 'Thermal modelling and experimental assessment of dependence of PV module temperature on wind velocity and direction, module orientation and inclination', *Sol. Energy*, 2014, **107**, pp. 443–460
- [7] Subudhi, B., Pradhan, R.: 'A comparative study on maximum power point tracking techniques for photovoltaic power systems', *IEEE Trans. Sustain. Energy*, 2013, **4**, (1), pp. 89–98
- [8] Elobaid, L.M., Abdelsalam, A.K., Zakzouk, E.E.: 'Artificial neural network-based photovoltaic maximum power point tracking techniques: a survey', *IET Renew. Power Gener.*, 2015, **9**, (8), pp. 1043–1063
- [9] Wu, T.F., Chang, C.H., Lin, L.C., et al.: 'Power loss comparison of single- and two-stage grid-connected photovoltaic systems', *IEEE Trans. Energy Convers.*, 2011, **26**, (2), pp. 707–715
- [10] Gao, S., Barnes, M.: 'Phase-locked loop for AC systems: analyses and comparisons'. Proc. IET Int. Conf. on Power Electronics, Machines and Drives, 2012, pp. 1–6
- [11] Timbus, A.V., Ciobotaru, M., Teodorescu, R., et al.: 'Adaptive resonant controller for grid-connected converters in distributed power generation systems'. Proc. IEEE Applied Power Electronics Conf. and Exposition, 2006, pp. 1601–1606
- [12] Agarwal, R., Hussain, I., Singh, B.: 'LMF based control algorithm for single stage three-phase grid integrated solar PV system', *IEEE Trans. Sustain. Energy*, 2016, **7**, (4), pp. 1379–1387
- [13] Pradhan, S., Hussain, I., Singh, B.: 'Modified VSS-LMS-based adaptive control for improving the performance of a single-stage PV-integrated grid system'. IET Science and Measurement Technology, Early Access
- [14] Jain, C., Singh, B.: 'Single-phase single-stage multifunctional grid interfaced solar photo-voltaic system under abnormal grid conditions', *IET Gener. Transm. Distrib.*, 2015, **9**, (10), pp. 886–894

- [15] Singh, B., Shahani, D.T., Verma, A.K.: 'Neural network controlled grid interfaced solar photovoltaic power generation', *IET Power Electron.*, 2014, **7**, (3), pp. 614–626
- [16] Liu, J., Miura, Y., Ise, T.: 'Power quality improvement of microgrids by virtual synchronous generator control', *Electr. Power Qual. Supply Reliab.*, Tallinn, Estonia, 2016, pp. 119–124
- [17] Deo, S., Jain, C., Singh, B.: 'A PLL-less scheme for single-phase grid interfaced load compensating solar PV generation system', *IEEE Trans. Ind. Inf.*, 2015, **11**, (3), pp. 692–699
- [18] Sayin, M.O., Vanli, N.D., Kozat, S.S.: 'A novel family of adaptive filtering algorithms based on the logarithmic cost', *IEEE Trans. Signal Process.*, 2014, **62**, (17), pp.4411–4424
- [19] Singh, B., Chandra, A., Al-Haddad, K.: '*Power quality: problems and mitigation techniques*' (John Wiley & Sons, Oxford, 2015)
- [20] 'IEEE recommended practice and requirement for harmonic control on electric power system', IEEE std. 519, 2014
- [21] 'IEEE guide for voltage Sag Indices', IEEE std. 1564, 2014, pp.1–59